A PRECISE APPROACH FOR RECOVERING POSES OF DISTAL LOCKING HOLES FROM SINGLE CALIBRATED X-RAY IMAGE FOR COMPUTER-ASSISTED INTRAMEDULLARY NAILING OF FEMORAL SHAFT FRACTURES

Guoyan Zheng and Xuan Zhang
MEM Research Center – ISTB, University of Bern, Stauffacherstrasse 78, CH-3014, Bern, Switzerland

Keywords: Model-based fitting, parameter decomposition, computer-assisted intramedullary nailing.

Abstract: One of the most difficult steps of intramedullary nailing of femoral shaft fractures is distal locking – the insertion of distal transverse interlocking screws, for which it is necessary to know the position and orientation of the distal locking holes of the intramedullary nail. This paper presents a precise approach for solving this problem using single calibrated X-ray image via parameter decomposition. The problem is formulated as a model-based optimal fitting process, where the to-be-optimized parameters are decomposed into two sets: (a) the angle between the nail axis and its projection on the imaging plane, and (b) the translation and rotation of the geometrical models of the distal locking holes around the nail axis. By using a hybrid optimization technique coupling an evolutionary strategy and a local search algorithm to find the optimal values of the latter set of parameters for any given value of the former one, we reduce the multiple-dimensional model-based optimal fitting problem to a one-dimensional search along a finite interval. We report the results of our *in vitro* experiments, which demonstrate that the accuracy of our approach is adequate for successful distal locking of intramedullary nails.

1 INTRODUCTION

It has been recognized that one of the most difficult steps of intramedullary nailing of femoral shaft fractures is distal locking – the insertion of distal interlocking screws, for which it is necessary to know the positions and orientations of the distal locking holes (DLHs) of the intramedullary nail (IMN). Complicating the process of locating and inserting the distal interlocking screw is the nail deformation with insertion. It has been reported that deformation occurs in several planes due to medial-lateral (ML) and anterior-posterior (AP) flexion of the distal nail after it has been inserted. Using a magnetic tracking system in a cadaveric study, Krettek *et al.* (1998) reported following deformation measurement results for small-diameter nails and large-diameter nails, respectively: lateral translations of 18.1 ± 10.0 mm and 21.5 ± 7.9 mm, dorsal translations of -3.1 ± 4.3 mm and 0.4 ± 9.8 mm, and rotation about the longitudinal axes of -0.1 ± 0.2 degrees and 10.0 ± 3.1 degrees. The reason for the wide variations of the insertion-related femoral nail deformation is due to the fact that the nail has to deform to the shape of the medullary canal upon insertion. The shape of the canal varies widely from person to person. It is not possible to predict how the nail will deform accordingly. Therefore, it is very difficult, to determine what the resultant locations and orientations of the DLHs will be relative to their initial position before it is deformed. The surgeon depends heavily on intra-operative X-ray means in a conventional surgical procedure for providing precise locations and orientations of the DLHs. It requires positioning the axis of the fluoroscope perpendicular to the locking holes so that these holes appear perfectly circular in the images. This is achieved through a trial-and-error method and requires long time X-ray exposure for both the surgeon and patient. It has been reported that the surgeon's direct exposure to radiation for each conventional surgical procedure was 3 – 30 min, of which 31% - 51% was used for distal locking (Sajeldal and Backe 1987).

The desire to target accurately with as little as possible X-ray exposure has led to various attempts

Zheng G. and Zhang X. (2007).
A PRECISE APPROACH FOR RECOVERING POSES OF DISTAL LOCKING HOLES FROM SINGLE CALIBRATED X-RAY IMAGE FOR COMPUTER-ASSISTED INTRAMEDULLARY NAILING OF FEMORAL SHAFT FRACTURES.
In *Proceedings of the Second International Conference on Computer Vision Theory and Applications*, pages 120-127
DOI: 10.5220/0002066101200127

to develop image-based methods for recovering the positions and orientations of DLHs (Zhu *et al.* 2002, Leloup *et al.* 2004, Yaniv and Joskowicz 2005). These methods require either multiple calibrated images or single image but with perfectly circular holes in the image, which normally requires the X-ray technician to use a try-and-move method several times to achieve.

This paper presents a precise approach for solving this problem using single calibrated fluoroscopic image via parameter decomposition. We do not ask for an image with perfectly circular holes but we do put a constraint on its acquisition, i.e., the reduced patient shaft should be roughly parallel to the image intensifier (II) of the fluoroscopy machine, which is much easier to be achieved intraoperatively. We then formulate the pose recovery of the DLHs as a model-based fitting problem and decompose the to-be-optimized parameters into two sets: (a) the angle between the nail axis and its projection on the imaging plane, and (b) the translation and rotation of the geometrical models of the DLHs around the nail axis. By using a hybrid optimization technique (Zheng *et al.* 2006) coupling an evolutionary strategy and a local search algorithm to find the optimal values of the latter set of parameters for each give value of the former one, we reduce the multiple-dimensional optimal fitting problem to a one-dimensional search along a finite interval.

The paper is organized as follows. Section 2 describes image calibration, geometrical models, and preprocessing. In Section 3, we describe the proposed approach in details. Section 4 presents our *in-vitro* experimental results, followed by conclusions in Section 5.

2 IMAGE CALIBRATION, GEOMETRICAL MODEL AND PREPROCESSING

2.1 Image Calibration

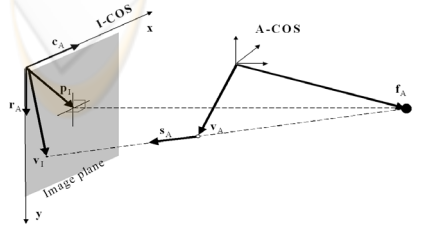

Figure 1: Weak-perspective pin-hole camera model.

In reality, the proximal fragment, the distal fragment, and the nail may be treated as three rigid bodies and registered independently. The rigid transformations between these three rigid bodies can be trivially obtained from a navigator such as an optoelectronic tracker, a magnetic tracker, or even a medical robot (Langlotz and Nolte 2004). As this is not our focus in this paper, here we assume that the fractured femur has already been reduced and the proximal fragment and distal fragment are kept fixed relative to each other at the time of image acquisition. We also assume that the nail has been inserted till the distal end of the femur and has been locked proximally by screw so that the complete femur and the nail can be treated as one rigid body. A local coordinate system (COS) is established on this rigid body through a so-called dynamic reference base (DRB) technique (Nolte *et al.* 1995). In the following description, let's denote this patient COS as $A-COS$. All computations are done in this reference COS.

To relate a pixel in the two-dimensional (2D) projection image to $A-COS$, the acquired image has to be calibrated for physical projection properties and be corrected for various types of distortion. We have chosen a weak-perspective pin-hole camera model as shown in Figure 1 for modeling the C-arm projection (Gremban *et al.* 1988). Using such a camera model, a 2D pixel $\mathbf{V}_\mathrm{I}$ is related to a three-dimensional (3D) point $\mathbf{V}_\mathrm{A}$ by following equations:

$$\mathrm{S_A} = \frac{(\mathrm{V_A} - \mathrm{f_A})}{\|\mathrm{V_A} - \mathrm{f_A}\|};$$

$$\begin{bmatrix} \mathrm{V_{I},}x \\ \mathrm{V_{I},}y \\ 1 \end{bmatrix} = \begin{bmatrix} \mathrm{c_{A},}x & \mathrm{c_{A},}y & \mathrm{c_{A},}z & \mathrm{p_{I},}x \\ \mathbf{r}_{\mathrm{A},x} & \mathbf{r}_{\mathrm{A},y} & \mathbf{r}_{\mathrm{A},z} & \mathrm{p_{I},}y \\ 0 & 0 & 0 & 1 \end{bmatrix} \begin{bmatrix} \mathrm{S_{A},}x \\ \mathrm{S_{A},}y \\ \mathrm{S_{A},}z \\ 1 \end{bmatrix} \quad (1)$$

where $\|\cdot\|$ means to calculate the length of a vector and the vectors $\mathbf{f}_\mathrm{A}$, $\mathbf{r}_\mathrm{A}$, $\mathbf{c}_\mathrm{A}$ and $\mathbf{p}_\mathrm{I}$ represent the position of focal point, the vector along image row increasing direction, the vector along image column increasing direction, and the 2D position of piercing point, respectively. They are projection parameters used to describe the projection properties of the C-arm and need to be calibrated preoperatively

Eq. (**1**) can be used for both forward and backward projections. For example, if we want to calculate the direction $\mathbf{S}_A$ of the forward projection ray of an image point $\mathbf{V}_\mathrm{I}$, an additional constraint $\|\mathbf{S}_A\| = 1$ can be used together with Eq. (**1**) to solve for it. The forward projection ray of point $\mathbf{V}_\mathrm{I}$ is defined by the focal point and the direction.

The position of the imaging plane in $A-COS$ and the focal length in our camera model is implicitly determined using the calibrated focal point $\mathbf{f}_A$ and the vectors $\mathbf{r}_A$ and $\mathbf{c}_A$. Any 2D image point $\mathbf{V}_I$ corresponds to a 3D spatial point $\mathbf{I}_A$ in this imaging plane, which is the intersection between its forward projection ray and this plane.

2.2 Geometrical Models

The distal part of IMN containing the two DLHs, which is what we are interested in, is modeled as a cylinder (Figure 2, left). The distance L between the centers of the two DLHs can be accurately extracted from its product information. The geometrical model of each DLH is represented by two circles as shown by Figure 2, right, and is used later to simulate X-ray projection of the DLH model.

To obtain the coordinates of those points (visualized as red dots in Figure 2, right) used to describe the model of the DLH, a local COS $C'uvw$ is established by taking the intersection point C (it is also called the center of the DLH) between the axis of the DLH and the axis of the IMN as the origin, the axis of the IMN as the u axis, and the axis of the DLH as the v axis (see Figure 2 for details).

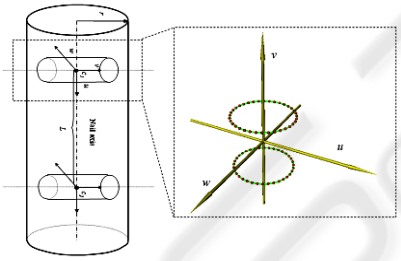

Figure 2: The geometrical model of the distal part of the IMN (left) and the geometrical model of the DLH (right).

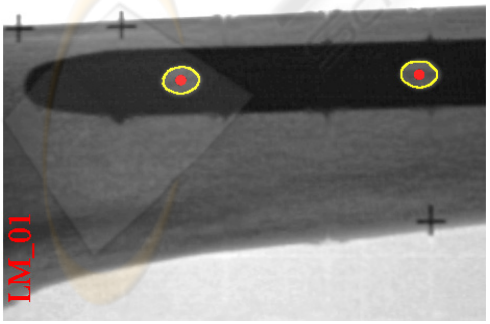

Figure 3: Feature point detection. The detected projection points (red dots) of the centers of both DLHs are displayed together with the edge pixels of the DLHs (yellow).

The coordinates of those points expressed in this local COS can be directly measured from the nail using a caliber, thanks to the symmetrical property of the DLH; or extracted from the engineering drawings of the nail, if they are available.

2.3 Preprocessing

The task of the preprocessing is to determine the projection points of the centers of the DLHs. To extract these feature points from the image, Hough transform (Jain and Schunk 1995) is used to find the two mostly parallel edge lines of the projection of the distal part of the IMN after applying a Canny edge detector to the image. The projection of the axis of the distal part of the IMN is considered as the middle line between these two mostly parallel edge lines. To determine those edge pixels belonging to DLHs, the method reported in (Yaniv and Joskowicz 2005) is modified for our purpose. A parallelpiped window, whose sizes are equal to the distance between the detected edge lines, is swept along the middle line to find two locations which contain the maximum number of edge pixels and whose distance is greater than a pre-selected distance threshold T (e.g. the width of the window). The centroids of the detected edge pixels in both locations are then calculated. The projection of the center of each DLH is then determined by finding the closest point on the middle line to the associated centroid. An example of feature point detection is shown in Figure 3.

3 THE PROPOSED APPROACH

3.1 Model-based Fitting for Pose Recovery

Using above detected feature points, we can find their corresponding spatial points on the imaging plane. Let's denote them as d_1 corresponding to the projection point of the center C_1 of the distal DLH (the DLH that is closer to the nail tip), and d_2 corresponding to the projection point of the center C_2 of the proximal DLH, respectively, as shown in Figure 4. These two points define a line in A-COS. This line together with the focal point f defines a plane where the axis of the distal part of the nail should fall in. As we know the coordinates for point f, d_1, and d_2, we can calculate three internal angles ω_1, ω_2, and ω_3 of triangle fd_1d_2. Assume the angle between the nail axis and its projection in the

imaging plane is α, then the coordinates of the centers of both DLHs are calculated as following:

$$C_1 = f + L_1 \cdot \frac{(d_1 - f)}{\| d_1 - f \|}; \quad C_2 = f + L_2 \cdot \frac{(d_2 - f)}{\| d_2 - f \|}$$
$$L_1 = L \cdot \frac{\sin(\omega_2 + \alpha)}{\sin(\omega_3)} \qquad (2)$$
$$L_2 = L \cdot \frac{\sin(\omega_2 + \alpha) \cdot \cos(\omega_3)}{\sin(\omega_3)} + L \cdot \cos(\omega_2 + \alpha)$$
$$where \quad \alpha \in (-\pi/2, \pi/2)$$

where L is the distance between the centers of two DLHs. It can be measured or extracted from the product information.

According to equation (2), the coordinates of both centers only depends on the parameter α, so as the direction of the nail axis (n_x, n_y, n_z).

Assuming that the coordinates of the center C of one of the DLHs is denoted as $[C_x, C_y, C_z]^T$, the problem to estimate the pose of the DLH in *A-COS* is now changed to find the rotation angle α, rotation angle θ, and translation distance δ of the geometrical model of the DLH along the nail axis $[n_x, n_y, n_z]^T$ so that the simulated X-ray projection of the DLH can be fitted to its real X-ray projection (see Figure 4 for details). This constrained transformation around the parameterized nail axis could be described by a 3×3 rotation matrix $rot(\alpha, \theta, \delta)$

$$\begin{bmatrix} n_x^2+(n_y^2+n_z^2)\cos(\theta) & n_x n_y(1-\cos(\theta))-n_z\sin(\theta) & n_x n_z(1-\cos(\theta))+n_y\sin(\theta) \\ n_x n_y(1-\cos(\theta))+n_z\sin(\theta) & n_y^2+(n_x^2+n_z^2)\cos(\theta) & n_y n_z(1-\cos(\theta))-n_x\sin(\theta) \\ n_x n_z(1-\cos(\theta))-n_y\sin(\theta) & n_y n_z(1-\cos(\theta))+n_x\sin(\theta) & n_z^2+(n_x^2+n_y^2)\cos(\theta) \end{bmatrix} \qquad (3)$$

and a translational vector $trans(\alpha, \theta, \delta) = [t_x, t_y, t_z]^T$:

$$\begin{cases} t_x = (C_x+\delta\cdot n_x)\cdot(n_y^2+n_z^2) - n_x\cdot((C_y+\delta\cdot n_y)\cdot n_y + (C_z+\delta\cdot n_z)\cdot n_z) + \\ \quad (n_x\cdot((C_y+\delta\cdot n_y)\cdot n_y + (C_z+\delta\cdot n_z)\cdot n_z) - (C_x+\delta\cdot n_x)\cdot(n_y^2+n_z^2))\cos(\theta) + \\ \quad ((C_y+\delta\cdot n_y)\cdot n_z - (C_z+\delta\cdot n_z)\cdot n_y)\sin(\theta) \\ t_y = (C_y+\delta\cdot n_y)\cdot(n_x^2+n_z^2) - n_y\cdot((C_x+\delta\cdot n_x)\cdot n_x + (C_z+\delta\cdot n_z)\cdot n_z) + \\ \quad (n_y\cdot((C_x+\delta\cdot n_x)\cdot n_x + (C_z+\delta\cdot n_z)\cdot n_z) - (C_y+\delta\cdot n_y)\cdot(n_x^2+n_z^2))\cos(\theta) + \\ \quad ((C_z+\delta\cdot n_z)\cdot n_x - (C_x+\delta\cdot n_x)\cdot n_z)\sin(\theta) \\ t_z = (C_z+\delta\cdot n_z)\cdot(n_x^2+n_y^2) - n_z\cdot((C_x+\delta\cdot n_x)\cdot n_x + (C_y+\delta\cdot n_y)\cdot n_y) + \\ \quad (n_z\cdot((C_x+\delta\cdot n_x)\cdot n_x + (C_y+\delta\cdot n_y)\cdot n_y) - (C_z+\delta\cdot n_z)\cdot(n_x^2+n_y^2))\cos(\theta) + \\ \quad ((C_x+\delta\cdot n_x)\cdot n_y - (C_{yz}+\delta\cdot n_y)\cdot n_x)\sin(\theta) \end{cases} \qquad (4)$$

The pose recovery problem can then be formulated as an optimal model-based fitting:

$$\min_{\{\alpha^*, \theta^*, \delta^*\}} \sum_i \| e_{j=CP(i)} - P(rot(\alpha,\theta,\delta)\cdot m_i + trans(\alpha,\theta,\delta)) \|^2 \qquad (5)$$

where $\{e_j\}$ are the detected edge pixels of the DLHs; $\{m_i\}$ are the points used to describe the geometrical models the DLHs; $P(.)$ denotes the projection operator; $CP(.)$ denotes the action of finding the closest edge pixel of the simulated projection point into the image of a model point.

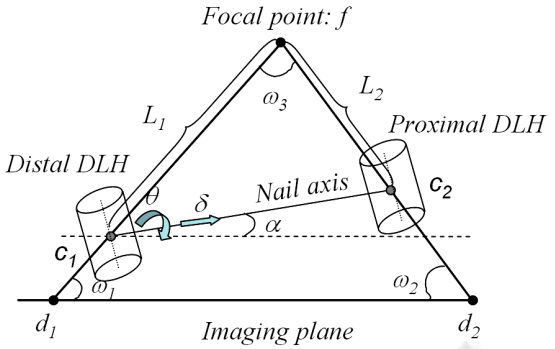

Figure 4: Schematic view of model-based fitting.

3.2 Parameter Estimation

Various techniques have been proposed for estimating parameters for model-based fitting. Lowe (1991) suggests to minimize the non-linear error function on image domain, where the perpendicular distance between projected model line and extracted edge point will be minimized. The correspondence between the model projection to image edge is found by selecting the one who has the shortest perpendicular distance. This strategy can lead to some ambiguity in fitting process when part of the model line has been occluded by structure of the model itself. This problem was solved by Fua (1996) through applying hidden algorithm to avoid this pitfall. All these algorithms suffer from the facts that they are easily to be trapped by a local minimum and that the interpretation and initialization of model parameter values have to be done by the operator, which is not desirable for an intra-operative application in a sterilized environment.

Parameter decomposition approach is a powerful optimization method that tries to decompose a high-dimensional problem into small, low-dimensional components and estimate the parameters for each component separately, thus reducing the computational complexity. The general idea of model decomposition for parameter estimation has bee successfully applied in many domains, e.g., geometrical curve fitting (Jiang and Cheng 2005) and Bayesian model learning (Neapolitan 2003).

According to our observation that the size of the geometrical models of the DLHs (around 10 mm in each dimension) is relatively small compared to the focal length of the X-ray image (around 1000mm), we decompose the control parameters in Eq. (5) into two sets: (a) the angle α between the nail axis and its projection in the imaging plane; and (b) the rotation and translation distance of the geometrical models of

the DLHs along the nail axis (θ, δ). Now the original optimization problem can be re-formulated as:

$$\min_{\alpha^*}[(\min_{\{\theta^*,\delta^*\}}\sum_i \| e_{j=CP(i)} - P(rot(\alpha,\theta,\delta)\cdot m_i + trans(\alpha,\theta,\delta))\|^2)] \quad (6)$$

Where the term in the square brackets simply means the minimum sum of distance for a fixed α and all possibilities of (θ, δ). The advantage of such decomposition lies in the fact that the latter set of variables can be calculated by using a hybrid optimization technique coupling an evolutionary strategy and an iterative closest projection point algorithm (ICPP) as proposed in our previous work (Zheng *et al.* 2006), which then reduces the original multiple-dimensional optimization problem to a one-dimensional search in a finite interval.

3.2.1 Initialization

Given a fixed α, we can estimate the positions of both centers of DLHs and the orientation of the nail axis. Then, the initial transformation between the local COS of the geometrical model of the DLHs and *A-COS* can be obtained by taking the estimated center as the origin, the estimated nail axis as the *u* axis, and the normal of the imaging plane as the *v* axis. All points defined in the local COS of the geometrical model of the DLH can then be transformed to *A-COS* using this transformation. The optimal values of the rotation θ and the translation δ of the models along the nail axis can be optimally estimated by fitting the geometrical models of the DLHs to the image as by a hybrid optimization technique as described below

3.2.2 The Iterative Closest Projection Point (ICPP) Algorithm

Let's denote E be a set of N_E detected 2D edge pixels $\{e_1, e_2, ..., e_{N_E}\}$ of the DLH projection. Further denote M^{t-1} be a set of N_M model point $\{m_0^{t-1}, m_1^{t-1}, ..., m_{N_M}^{t-1}\}$ at iteration step *t-1*. Now in the iteration step *t*, we perform following steps:

Simulating X-ray projection: In this step, we simulate the X-ray projection of the geometrical models of the DLHs to remove invisible points. Let P^{t-1} be a set of N_P 2D projection points $\{p_1^{t-1}, p_2^{t-1}, \cdots, p_{N_P}^{t-1}\}$ obtained by simulating X-ray projection of 3D model into the image. Normally $N_P << N_M$. Thus, for each 2D projection point p_i^{t-1}, we know its associated 3D model point m_i^{t-1}.

Find closest projection point: In this step, we try to find the closest neighbor edge pixel e_i of each 2D model projection point p_i^{t-1}.

Establishing 3D-2D correspondence: For each 2D matched pairs (e_i, p_i^{t-1}), calculate the forward projection ray BP_i of the 2D edge pixel e_i. Then for the ray BP_i, calculate a 3D point pair $PP_i^{t-1} = (be_i^{t-1}, m_i^{t-1})$, where be_i^{t-1} is a point on the line BP_i that is closest to the 3D model point m_i^{t-1} of the model projection point p_i^{t-1}.

Estimating pose: For all calculated 3D point pairs $PPS^{(t-1)} = \{PP_i^{t-1}\}$, find an optimal local solution of all pose parameters by minimizing following disparity function $S(\theta^{(t-1)}, \delta^{(t-1)})$:

$$\underset{\{\theta^{(t-1)*},\delta^{(t-1)*}\}}{\mathbf{argmin}}\ S(\theta^{(t-1)}, \delta^{(t-1)})$$
$$S(\theta^{(t-1)}, \delta^{(t-1)}) = \sum_i \| be_i^{t-1} - (rot(\theta^{(t-1)}, \delta^{(t-1)})\cdot m_i^{t-1} + trans(\theta^{(t-1)}, \delta^{(t-1)})\|^2 \quad (7)$$

where we drop the symbol α from the expressions, as its value is fixed.

These steps are repeated until all pose parameters are converged.

3.2.3 The Evolutionary Strategy

The ICPP algorithm can be regarded as a local minimum search algorithm but we are trying to find the global minimum of the disparity function that may be well hidden among many poorer local minima. In our approach, this is handled by combining a conventional genetic algorithm (Goldberg 1989) with the ICPP algorithm. The genetic algorithm acts as a random generator for possible parameter sets that solve the minimization problem. All generated individual parameter set is then fed through the ICPP algorithm before being rated using the disparity function. Five best ones become the parents of next generation. The algorithm stops when the differences of the disparity function values of all five best ones are smaller than a pre-selected threshold.

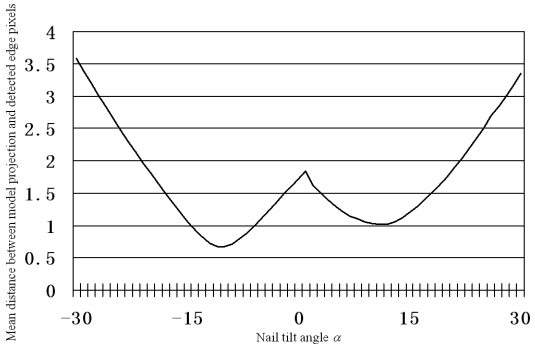

Figure 5: Optimization space of the nail tilt angle α.

3.2.4 Optimization of Parameter α

We now convert a multiple-dimensional optimization problem to a one-dimensional one, where the parameter α can be optimized by a search along a finite interval [-30°, +30°] (due to the acquisition constraint that we put). A typical optimization space of this parameter is shown in Figure 5. It has a symmetrical shape and a clear global optimum around the ground truth $\alpha=10.4^{o}$. We could separate the optimization space into two sub-intervals, i.e. [-30°, 0) and [0, 30°]. In each sub-interval, the optimum of that sub-interval could be easily found by a local search algorithm starting from any initialization value. Actually, in all experiments, we have simply initialized α by the middle value of each sub-interval. The global minimum is then found by taking the better one of the two optima.

4 EXPERIMENTAL RESULTS

We designed and conducted two experiments to analyze the accuracy and robustness of the proposed approach. A SYNTHES® (STRATEC Medical, Oberdorf, Switzerland) 9 mm solid titanium femoral nail was used in our study. A Siemens ISO-C^{3D} C-arm (Siemens AG, Erlangen, Germany) was used to acquire fluoroscopic images for our experiments.

In the first experiment, the nail was inserted into a cadaveric human femur and was locked proximally. The ground truth of the positions of the DLHs was obtained after image acquisition by inserting a custom-made steel rod through the hole and then digitizing both top and bottom centers of the rod using an optically trackable sharp pointer (OPTOTRAK 3020, Northern Digital Inc, Waterloo, Canada).

Three images acquired from different view directions were used in our experiments, as shown in Figure 6. For each image, we applied the proposed approach ten times to estimate the poses of the DLHs. The estimated results were compared to the ground truth to compute the errors for each DLH, which were defined as the angular difference between the estimated hole axis and the one obtained through pointer-based digitization, and the positional difference of the entry point and its ground truth along the plane perpendicular to the hole axis (obtained by projecting the difference vector into the plane perpendicular to the hole axis), because the positional deviation along the hole axis is not important for the task of insertion of distal locking screw

In all studies, the poses of DLHs could be automatically recovered. The angular and positional errors are shown in Table I. Compared to ground truths, the average angular error was found to be 1.0° (std=0.4°) and the average positional error along the plane perpendicular to the hole axis was found to be 0.6 mm (std=0.4 mm).

In the second experiment, a test bench was designed and implemented, which allowed rotation and tilt of the test subject, as shown in Figure 7. The nail was inserted tightly into the plastic bone and was locked proximally. The plastic bone together with the nail was then fixed to the test bench. A dynamic reference base was fixed to the bone to establish a local coordinate system. The ground truths of the direction of the nail axis as well as the positions of the centers of the DLHs and the directions of the axes of the DLHs were obtained from a registration-free 3D-navigation system [4] using the SIREMOBIL ISO-C^{3D} Carm.

The reference position (rotation = 0°, tilt = 0°) was obtained using a try-and-move method until the projections of both holes appeared perfectly circular. We then tilted the test subject with an interval of 5° until 25°. At each tilted position, we rotated the test subject with an interval of 5° until 25°, which results in totally 6x6 = 36 configurations. For each configuration (tilt, rotation), a lateral-medial image was acquired.

We applied the present approach to these 36 images. For each image, we compared the estimated results to the ground truths. We computed the angular error of the estimated nail axis and the angular errors of the estimated axes of the DLHs. And to get a clear idea how the positional errors were distributed, we decomposed the positional errors along the three orthogonal directions, i.e., the nail axis direction, the distal locking hole axis

direction, and the cross product of the former two directions.

It was found that angular errors in all configurations except for two configurations (25^o, 20^o) and (25^o, 25^o) were smaller than 1.8^o. The positional errors along the distal locking hole axis were bigger than those errors along other two directions. When the tilt was smaller than 25^o and when the rotation was smaller than 25^o, the average angular error in estimating the nail axis was found to be 0.5^o (std=0.2^o, max=1.2^o), the average angular error in estimating the axes of the DLHs was found to be 0.7^o (std=0.3^o, max=1.5^o), the average positional error along the nail axis direction was found to be 0.3 mm (std=0.4 mm, max=1.4 mm), the average positional error along the distal locking hole axis direction was found to be 1.3 mm (std=1.7 mm, max=7.9 mm), and the average positional error along the cross product direction was found to be 0.4 mm (std=0.5 mm, max=2.5 mm).

5 CONCLUSIONS

We have presented a novel variable decomposition approach for automatic pose recovery of distal locking holes from single calibrated fluoroscopic image. Unlike previously introduced method (Yaniv and Joskowicz 2005), our approach does not ask for an image with perfectly circular holes. Our *in vitro* experimental results demonstrate that the accuracy of our approach is adequate for successful distal locking of intramedullary nails.

REFERENCES

Krettek C., Mannβ J., Miclau T., et al. (1998) Deformation of femoral nails with intramedullary insertion. *J Orthop Res*, 16(5): 572 – 575.

Skjeldal S. and Backe S. (1987) Interlocking medullary nails – radiation doses in distal targeting. *Arch Orthopaedic Trauma Surg*, 106: 179 – 181.

Zhu Y., Phillips R., Griffiths J.G., et al. (2002) Recovery of distal hole axis in intramedullary nail trajectory planning. *Proc Inst Mech Eng [H]*, 216(5): 323 – 332.

Leloup T., Schuind F., and Warzee N. (2004) Process for the acquisition of information intended for the insertion of a locking screw into an orifice of an endomedullary device. *European Patent Application Number*: 04447153.0.

Yaniv Z. and Joskowicz L. (2005) Precise robot-assisted guide positioning for distal locking of intramedullary nails. *IEEE T Med Imaging*, 24(5): 624 – 635.

Zheng G., et al. (2006) A robust and accurate two-stage approach for automatic recovery of distal locking holes in computer-assisted intramedullary nailing of femoral shaft fractures. Submitted to *IEEE T Med Imaging*.

Langlotz F. and Nolte L.-P. (2004) Technical approaches to computer-assisted orthopedic surgery. *Eur J Trauma*, 30(1): 1– 11.

Nolte L.-P., Visarius H., Arm E. et al. (1995) Computer-aided fixation of spinal implants. J Image Guid Surg, 1: 88 – 93.

Gremban K.D., Thorpe C.E., Kanade T. (1988) Geometric camera calibration using systems of linear equations. In: Proceedings of IEEE conference on robotics and automation, pp. 562-567.

Jain R., Kasturi R., and Schunk B. G. (1995) Machine Vision. New York: McGraw-Hill.

Lowe F.G. (1991) Fitting parameterized three-dimensional models to images. IEEE T Pattern Anal, 13(5): 441-450.

Fua P. (1996) Model-based optimization: accurate and consistent site modeling. The 18th Congress, International Society for Photogrammetry and remote sensing, Vienna, Austria, pp. 222-223.

Jiang X. and Cheng D.C. (2005) A novel parameter decomposition approach to faithful fitting of quadric surfaces. Pattern Recognition: 27th DAGM Symposium, LNCS 3663, pp. 168-175

Neapolitan R.E. (2003), Learning Bayesian Networks. (1st Ed) Prentice Hall

Goldberg D.E. (1989) Genetic algorithms in search, optimization, and machine learning. Reading, MA, Addison-Wesley.

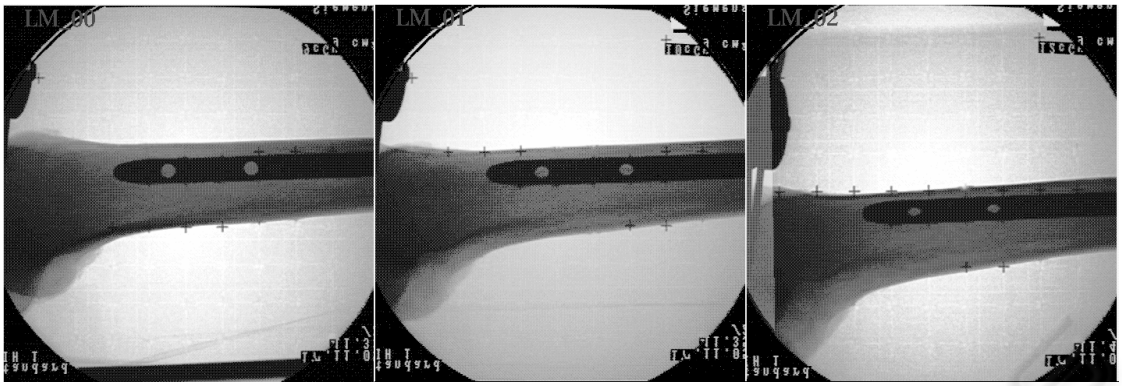

Figure 6: Three images used in our experiments. From left to right: LM_00, LM_01, and LM_02.

Table 1: Comparision results between the estimated poses of the distal locking holes and their associated ground truth.

Image	Angular differences (°)	Positional differences along the plane perpendicular to the hole axis (mm)
LM_00	0.7 ± 0.3	0.2 ± 0.0
LM_01	0.9 ± 0.2	0.4 ± 0.1
LM_02	1.5 ± 0.2	1.1 ± 0.1
Overall	1.0 ± 0.4	0.6 ± 0.4

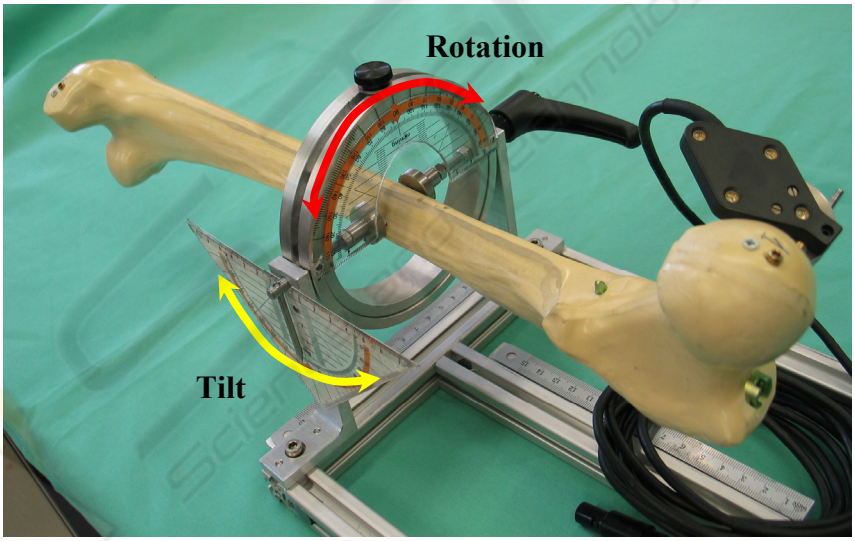

Figure 7: Test bench for evaluating the present approach.